

*Splash suppression during wafer wet
cleaning through drop penetration across
metal meshes and porous fiber mats*

**Chan-Woo Park, Tae-Gun Kim, Min-
Woo Kim, Ali Aldalbahi, Mohamed El-
Newehy & Sam S. Yoon**

Journal of Visualization

ISSN 1343-8875

J Vis

DOI 10.1007/s12650-019-00620-2



Your article is protected by copyright and all rights are held exclusively by The Visualization Society of Japan. This e-offprint is for personal use only and shall not be self-archived in electronic repositories. If you wish to self-archive your article, please use the accepted manuscript version for posting on your own website. You may further deposit the accepted manuscript version in any repository, provided it is only made publicly available 12 months after official publication or later and provided acknowledgement is given to the original source of publication and a link is inserted to the published article on Springer's website. The link must be accompanied by the following text: "The final publication is available at link.springer.com".



REGULAR PAPER

Chan-Woo Park · Tae-Gun Kim · Min-Woo Kim · Ali Aldalbahi · Mohamed El-Newehy · Sam S. Yoon

Splash suppression during wafer wet cleaning through drop penetration across metal meshes and porous fiber mats

Received: 31 May 2019 / Revised: 7 August 2019 / Accepted: 9 November 2019
© The Visualization Society of Japan 2019

Abstract Semiconducting silicon wafers were subjected to centrifugal wet cleaning to remove micro-contaminants. The circular wafers were rotated while a cleaning liquid was supplied to the wafer surface. During such a cleaning process, the centrifugal force atomizes the liquid film at the wafer edges, producing drops. These drops travel in the confined chamber, collide with the chamber walls, and form splashed droplets. Thereafter, the splashed droplets return to the wafer, thereby significantly increasing the risk of re-contamination. Given this wafer wet cleaning scenario, we experimentally investigated the trajectories of splashed droplets. We introduced metal mesh filtration and air-blowing techniques to minimize wafer re-contamination by the splashed droplets. The metal mesh decreased the speed of the drops, thus minimizing the intensity of splashing. The droplets were also air-blown with a supersonic stream to deflect the droplets from their trajectories and thus prevent them from reaching the wafer. The optimal air-blowing condition was determined through parametric studies. The metal mesh was electroplated with copper, producing textured surfaces on the mesh wires. In addition, the metal fiber mats were laminated on the metal mesh and the effects of these on splashing were studied. Further, photographs of droplets spreading and splashing over these metal meshes were captured to elucidate their detailed dynamics. Time-series snapshots of drops penetrating the metal meshes were also captured.

Keywords Splash · Drop impact · Wettability · Metal mesh · Metalized fiber mat · Supersonic blowing**List of symbols**

d_1	Distance from impact location to sensitive paper (horizontal) (mm)
d_2	Distance from disk edge to mesh (horizontal) (mm)
D	The spreading diameter (mm)
DM	Double layer meshes
D_{drop}	Diameter of drop (mm)
D_0	Initial diameter of drop (mm)
D_p	Mesh pore size (mm)
D_w	Mesh wire diameter (mm)
EP	Electroplating
h_1	Gap between mesh and acrylic wall (vertical) (mm)

Chan-Woo Park and Tae-Gun Kim have contributed equally.

Electronic supplementary material The online version of this article (<https://doi.org/10.1007/s12650-019-00620-2>) contains supplementary material, which is available to authorized users.C.-W. Park · T.-G. Kim · M.-W. Kim · S. S. Yoon (✉)
School of Mechanical Engineering, Korea University, Seoul 24801, Republic of Korea
E-mail: skyoon@korea.ac.krA. Aldalbahi · M. El-Newehy
Department of Chemistry, College of Science, King Saud University, Riyadh 11451, Saudi Arabia

Published online: 18 December 2019

h_2	Gap between sensitive paper bottom edge and disk top (vertical) (mm)
h_3	Distance between liquid nozzle exit to disk top (vertical) (mm)
H_1	Distance between liquid nozzle exit to mesh (vertical) (cm)
H_2	Distance between supersonic air nozzle to disk top (vertical) (cm)
N	The number of multiple drops
N_m	The number of meshes
Re	Reynolds number
SM	Single layer mesh
t	Interval time (s)
u_i	Drop impact speed (m/s)
W	Drop impact speed (%)
We	Weber number

Greek symbols

γ	Geometric ratio, $\gamma = 1 + D_w/D_p$
ρ	Liquid density (kg/m^3)
μ	Liquid dynamic viscosity (N s/m^2)
σ	Liquid surface tension (N/m)

1 Introduction

Contamination of semiconducting devices with organic and inorganic microparticle impurities is a major cause of their malfunction (Kern 1990; Hattori et al. 1998; Ryoo 2005a, b; Ruzyllo et al. 2007; Sato et al. 2012; Ruzyllo and Hattori 2014). These impurities or contaminants diffuse into the semiconducting devices during thermal treatments, thus causing device malfunctions. Therefore, semiconductor wafer surfaces should be cleaned to ensure and improve the performance and reliability of semiconducting devices.

Among various cleaning processes, spinning wet rinsing is widely used, whereby a columnar water jet is applied vertically on top of the rotating circular wafer (Kern 1990). The centrifugal force due to rotation generates a wavy liquid film on the wafer surface, thereby launching the water drops to the edge of the rotating wafer. The launched drops travel horizontally and eventually collide with the surrounding chamber wall. These impurity-containing drops shatter into splashed droplets upon impact with the wall and rebound to the rotating wafer, thereby re-contaminating the wafer. This impact scenario and the production of numerous splashed droplets are undesirable. Therefore, it is imperative to reduce splashing or/and deflect the trajectories of the splashed droplets to prevent or minimize the wafer re-contamination.

We introduced metal meshes of various pore sizes and metal fiber mats with microscale pores and allowed the drops to pass through these obstacles before impacting the chamber wall. These mesh/mat obstacles slow the drop motion and reduce the intensity of splashing. The introduction of multiple meshes approximates the installation of a porous medium that slows or stops the drops in motion before impact (Ryu et al. 2017; Xu et al. 2017; Boscarriol et al. 2018; Zhang et al. 2018). However, the complete removal of splashed droplets is virtually impossible because the drops collide with the mesh itself, thereby inducing minor splashing. For this reason, the thin wire minimizes the impact surface available to the moving drops and thus minimizes splashing. An optimal pore size facilitates smooth filtration of the drops and imposes sufficient drag to slow the drop motion. Therefore, we studied the effects of the pore size of the mesh and surface conditions of the wire on the intensity of droplet splashing. In addition, we aimed to deflect the splashed droplets from their trajectory by blowing air, thereby minimizing the wafer re-contamination.

Drop impact on metal meshes has recently received attention because it can be systematically and accurately controlled by the various pore sizes of the porous media or mesh. Porous substrates have drastically different wettability depending on their pore size and surface texture (Ryu et al. 2017; Xu et al. 2017; Boscarriol et al. 2018; Zhang et al. 2018; Lembach et al. 2010; Sahu et al. 2012, 2013, 2015). Therefore, superhydrophobicity or/and superhydrophilicity can be imparted by modifying the surface of the metal mesh (Ryu et al. 2017; Lembach et al. 2010). Lembach et al. (2010) provided details regarding water drops impact onto a solid substrate coated with porous nanofiber mats. They found the pinning effect at the maximum spreading stage, which prevented receding and thus fingering formation at the drop periphery. They also found that the mat having the pore size of $\sim 5 \mu\text{m}$ and the mat thickness of 100–200 μm were optimal to absorb water that facilitated pinning the contact line of a spreading drop as well as delivering water to the solid substrate. Sahu et al. (2012) studied the drop penetration across porous nanofiber mats. They found the liquids with a lower surface tension and viscosity penetrated the mats more easily and liquid penetration always set in if the impact velocity was high. This phenomenon was universally observed for all

types of the nanofiber mats; even the Teflon mat was incapable of preventing liquid penetration when the liquid surface tension and viscosity were low. Blowing drops off by gas flow along thin filaments was studied by Sahu et al. (2013). The physical phenomena of the blowing drops along thin filaments is similar to those of the drop impact against mesh wires. Sahu et al. (2015) also demonstrated that falling drops with sufficient dynamics can penetrate into both glass fiber and Teflon membranes, which were porous materials.

In general, drop impact on a mesh occurs in the order of deposition, partial imbibition, and eventual penetration with an increase in the kinetic energy of the drop. Drop penetration can be promoted with an increase in the impact velocity. Drop penetration decreases when the liquid viscosity is increased and the pore size is refined (Boscaroli et al. 2018). For example, if the pores are excessively small, only partial penetration of drop occurs and the remaining mass on the mesh forms a liquid pool, which completely changes the impact conditions for subsequent drops. This multiple-drop impact occurs in many industrial applications such as inkjet printing, spray-coating, fabrication of superhydrophobic textiles, water harvesting, anti-icing, anti-fouling, and heat-transfer enhancement via surface texturing (Ryu et al. 2017). However, existing studies of drop impact on metal meshes are limited to single-drop impact at a relatively low speed. Severe splashing conditions that produce numerous splashed droplets have not been considered so far.

The current study addresses the relatively high-speed impact of multiple drops, with guaranteed production of numerous splashed droplets. The splashed droplets were quantified by placing sensitive papers at various locations where the droplets fell. The splashing intensity is thus quantified accordingly. The various pore sizes of the mesh and the surface wettability state of the meshes resulted in different splashing conditions. This allowed us to identify the condition that yields the ideal scenario for reducing the risk of wafer contamination.

2 Experimental methods

2.1 Vertical drop impact

Figure 1a shows a water drop with diameter $D = 4.5$ mm released vertically from a piston needle using a syringe pump (Legato 100, kdScientific, USA). The impact speed of the drop is solely determined by gravity, while the impact of a horizontal drop shown in Fig. 1b is determined by the centrifugal force of the rotating wafer. The drop was released from heights (H_1) of 5, 20, and 65 cm, yielding experimental impact speeds (u_i) of 0.84, 1.66, and 3 m/s, respectively, at the substrate (mesh or solid wall).

Meshes with pore sizes D_p of 1.72, 1.09, and 0.22 mm and wire diameters D_w of 0.5, 0.5, and 0.14 mm were used; these are referred to as coarse, medium, and fine mesh, respectively. The corresponding geometric ratios, as defined by Boscaroli et al. (2018), are $\gamma = 1 + D_w/D_p = 1.29, 1.46,$ and $1.64,$ respectively. In addition, a mesh with the pore size D_p of 0.97 mm and the wire diameter D_w of 0.18 mm had the corresponding geometric ratio $\gamma = 1.18$. This particular mesh allowed relatively large pore sizes with thin wire sizes that facilitated smooth penetration of drops with minimized splashing.

The mesh was located approximately $h_1 = 0$ and 10 mm from a solid acrylic wall. After a drop was released from the piston from height H_1 , splashing occurred and droplets formed for the cases of $h_1 = 0$ and 10 mm. The splashed droplets travelled radially, with trajectories traced by the water-sensitive paper (20,301-3N, TeeJet technologies company, IL 60,139, USA) located at distance d_2 from the drop-impact location. All the reported wetting percentage data are averages from three repeated runs in each case, from which the error margin was estimated. The wetting percentage was computed by image processing of the dark area formed on the paper by the splashed droplets (*ImageJ* Software). The metal mesh was made of stainless steel electroplated with copper to induce superhydrophilicity; see the first scanning electron microscopy (SEM) image in Fig. 1c. This surface state of the textured mesh induces superhydrophilic interaction with static water drops, according to our water contact angle test (not shown here for brevity).

Electrospun nanofibers were sputter-coated with platinum to a thickness of a few nanometers to produce metallized fibers. This sputter coating was carried out to facilitate surface conductivity required to initiate electroplating. Then, a bare copper foil was immersed in an electroplating solution. Thereafter, a voltage of 1 V (electric current density, 67 mA/cm^2) was applied to the circuit during 30 s to electroplate the nanofibers coated with Pt; see the middle image in Fig. 1c. The metal mesh wires did not require platinum coating before electroplating, because they are electrically conductive. The metal mesh was immersed in the electroplating solution for 30 s to obtain the surface morphology shown in Fig. 1c (the left image). The

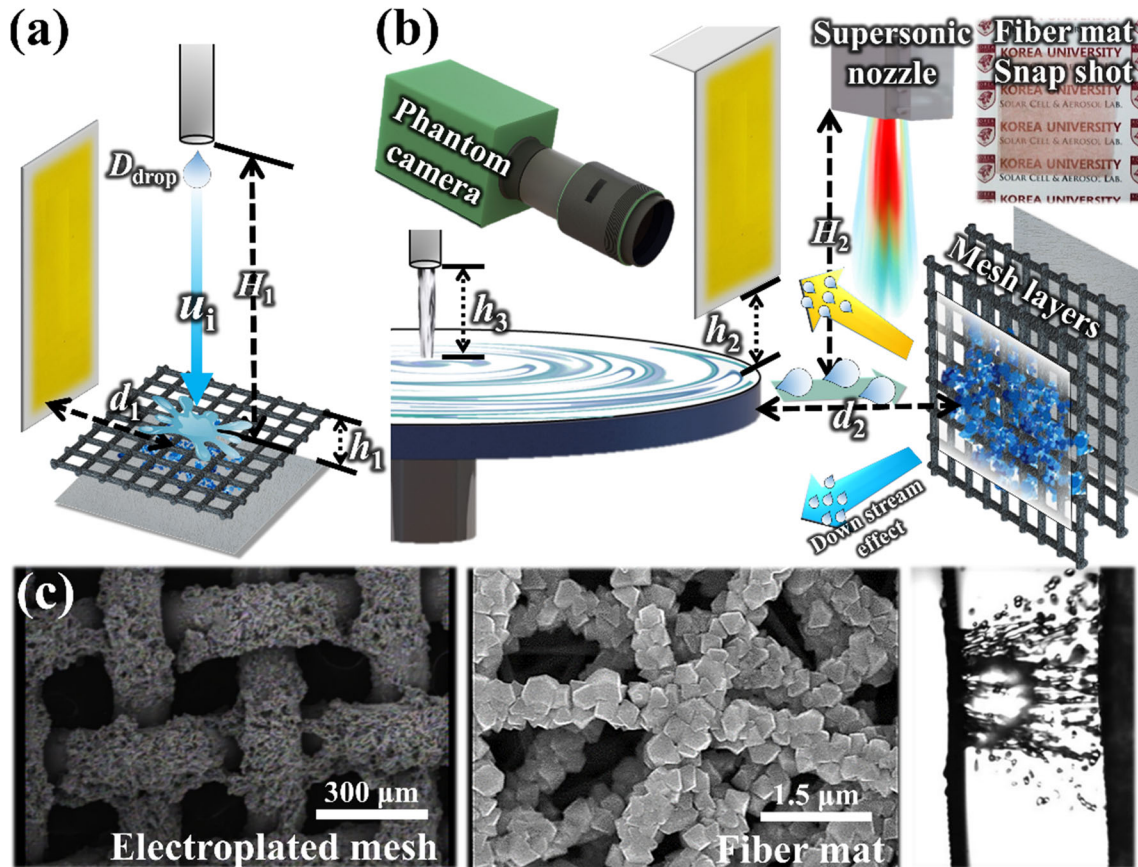


Fig. 1 Schematics illustrating **a** a vertical drop impact and **b** a horizontal drop impact. A rotating wafer on which a liquid film is formed imposes centrifugal force on the liquid film, which gets atomized at the wafer periphery. The atomized drops infiltrate the fiber mat and the metal mesh and then collide with the solid wall beneath. The splashed droplets rebounding and returning to the wafer are detected by the water-sensitive paper. **c** SEM images showing an electroplated stainless metal mesh (left) and electroplated metal fiber mat (middle), and a photograph of the drop impact phenomenon across the metal mesh (right)

details of the electroplating conditions may be found in our previous reports (Kim et al. 2017; Yoon et al. 2016; An et al. 2014, 2016).

2.2 Horizontal drop impact with air blowing

As shown in Fig. 1b, the wafer spinning at the speed of 300–500 rpm launches drops from its edge. The impact speed was estimated using photographs from a high-speed camera (Phantom 6117 M, Phantom, USA). In case of the horizontal setup in Fig. 1b, water was supplied to the rotating disk by a liquid column jet, whose nozzle was located at a height $h_3 = 45$ mm above the disk. The bottom of the sensitive paper that detected the splashed droplets was located at the edge of the disk at a distance $h_2 = 10$ mm above the disk. The supersonic nozzle that blew away the splashed droplets downward was located parallelly at $H_2 = 11$ cm above the disk. The mesh on which the drop impacts was located away from the disk edge at a distance ranging from $d_2 = 3$ to 13 cm.

These drops travel horizontally and first collide with the metal mesh covered with copper fiber mats (see the snapshot at top right). Owing to filtration through the mesh and mat, the speed of the drop is reduced before colliding with the solid wall. Note that in the scenario tested, the mesh was not in contact with the solid wall, but placed at a distance $h_1 = 10$ mm. The drops collide with the mesh/mat, splash, and bounce back toward the rotating wafer. To detect how far these bouncing splashed droplets travel, sensitive papers were placed at a distance d_2 . To minimize the wafer contamination caused by these splashed droplets, a supersonic nozzle was installed as depicted in Fig. 1b; the airflow from this nozzle deflects the splashed droplets from their original trajectories. The splashed droplets were blown downward by the supersonic

airstream. The operating pressure of the supersonic nozzle was varied from 1 to 5 bar, thus changing the air speed. The details of the supersonic nozzle may be found in previous reports (Lee et al. 2016, 2017; Kim et al. 2018).

3 Results and discussion

3.1 Vertical drop impact

Figure 2a shows the trace of the splashed droplets generated from drop impact corresponding to a release height of $H_1 = 65$ cm. The water-sensitive papers were located at $2 \leq d_1 \leq 9$ cm from the impact location. Drops were released for 30 s with a mass flow rate of 3 mL/min (or 5.1×10^{-5} kg/s), producing a total of 30–32 drops. A significant amount of splashed drops is observed when the paper is located closer to the impacting location, whereas fewer drops reach the paper when it is located at a larger d_1 .

Figure 3a shows data for drops released from heights $H_1 = 5, 20,$ and 65 cm, which yield drop impact speeds of $u_i = 0.84, 1.66,$ and 3 m/s, respectively, as estimated experimentally from videos recorded by a high-speed camera. The theoretical impact speeds of these drops calculated using $u_i = (2gH_1)^{1/2}$ are higher at $u_i = 1, 2,$ and 3.6 m/s. The differences between the theoretical and experimental values indicate that

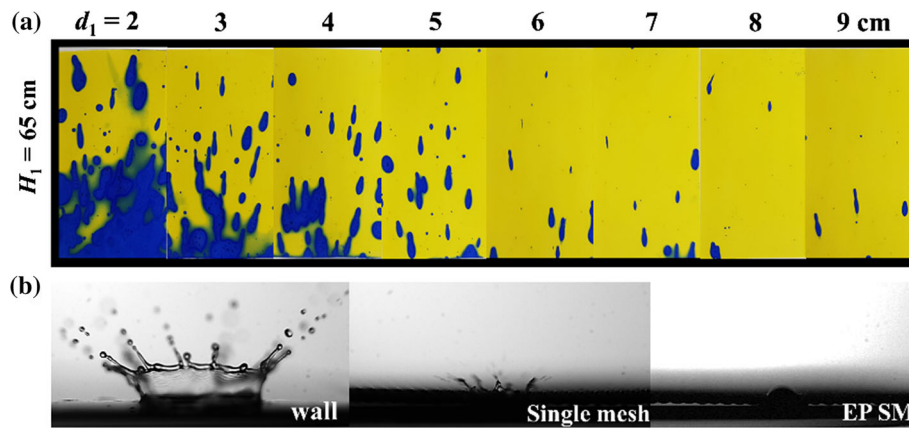


Fig. 2 **a** Traces of splashed droplets on water-sensitive papers placed at various distances (d) from the drop impact location. Impact speed $u_i = 3$ m/s. **b** Snapshots of drops released from $H_1 = 65$ cm colliding a solid wall (top), single mesh (middle), and EP SM (bottom), which are directly below the nozzle. Drop diameter was fixed at $D = 4.5$ mm for all cases. No air gap was present between the mesh (mat) and dry wall: $h_1 = 0$ mm. The geometric ratio of the medium mesh is $\gamma = 1.46$

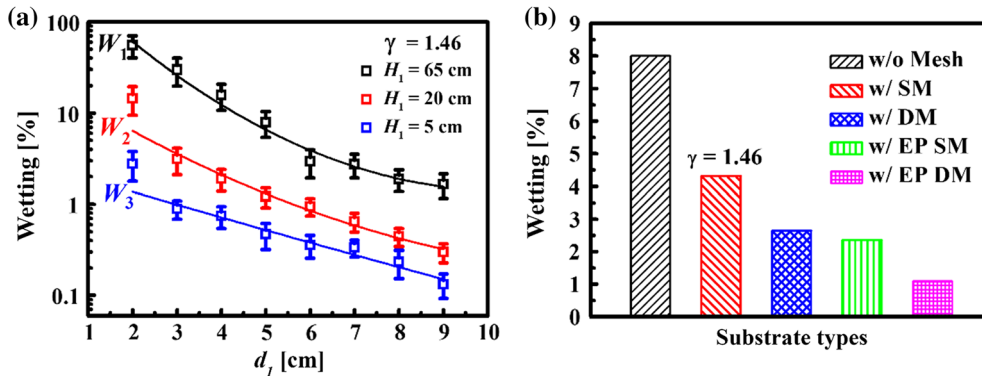


Fig. 3 **a** Wetting percentage of splashed droplets for $u_i = 0.84, 1.66,$ and 3 m/s ($H_1 = 5, 20,$ and 65 cm, respectively). **b** Wetting percentage of splashed droplets for various substrates: dry wall (w/o Mesh), single mesh (SM), double mesh (DM), electroplated single mesh (EP SM), and electroplated double mesh (EP DM). The impact conditions are $u_i = 3$ m/s, $H_1 = 65$ cm, and $d_1 = 5$ cm. No air gap was present between the mesh (mat) and dry wall: $h_1 = 0$ mm. The geometric ratio of the medium mesh is $\gamma = 1.46$

approximately 16–17% energy was lost owing to aerodynamic drag during the release. The results suggest that greater wetting occurs for higher H_1 or u_i and lower d_1 , as expected. Using the experimental values, the corresponding Weber numbers ($We = \rho D u_i^2 / \sigma$) were calculated to be 43, 169, and 553, respectively; the Reynolds numbers ($Re = \rho u_i D / \mu$) are 3375, 6670, and 12,053, respectively. These trends are correlated by the quadratic functions below for $H_1 = 65$, 20, and 5 cm, respectively, in conjunction with Fig. 3a

$$W_1 = 0.74d_1^2 - 11.91d_1 + 49.57 \quad (1)$$

$$W_2 = 0.06d_1^2 - 1.09d_1 + 5.42 \quad (2)$$

$$W_3 = 0.01d_1^2 - 0.29d_1 + 1.65 \quad (3)$$

Figure 3b shows the wetting percentages for different substrates obtained by fixing their lateral location at $d_1 = 5$ cm. The greatest wetting percentage (W) is observed for the dry wall. With a single mesh (SM), the splashing is reduced. When an extra metal mesh is layered on the existing mesh to obtain a double mesh (DM), splashing is reduced further. The metal mesh was electroplated (EP) with copper and then the wires constituting the mesh were textured with microstructures, as shown in the inset SEM images in Fig. 1c. This texturing of the wire surface increases the surface hydrophilicity, thus decreasing the droplet rebound. This phenomenon is shown in the bottom snapshot in Fig. 2b. Splashing was clearly suppressed using a textured wire mesh, as shown quantitatively by the wetting percentage in Fig. 3b.

Figure 4 shows time-series snapshots of drops colliding with various substrates, viz., a solid wall, metal mesh, and fiber mat. Figure 4a shows a drop spreading on a dry acryl solid wall, which has the static water contact angle of $WCA = 75^\circ$ (not shown here for brevity). A releasing liquid reservoir was dyed with a black ink. A backlight technique was used to provide sufficient lighting for the high-speed camera. An LED light was irradiated behind the acryl substrate, which distinguished falling black drops from background. It appears that the maximum spreading diameter is reached at $t = 5$ ms with fingers formed at the edge or rim of the spreading liquid film. These fingers arise from Rayleigh–Taylor instability (Drazin and Reid 2004) and they later merge; the number of fingers decreases with time t . An irregular liquid film rim is formed at $t = 11$ ms when the liquid film recedes and contracts.

Figure 4b shows a drop spreading on a fine metal mesh ($\gamma = 1.64$). The maximum spreading diameter is observed at approximately $t = 3$ ms, and then the drop recedes. Some of the jet fingers formed at the liquid periphery detach and roll along the metal mesh to points far from the bulk liquid film. This fluid behavior demonstrates the surface tension force that pulls the neighboring liquid. The same drop impact experiment was also carried out on a medium metal mesh. The spreading diameter was slightly larger because a relatively lower viscous drag was imposed. For a smaller pore size, the total surface area of the mesh penetrated by the spreading liquid was larger, which increased viscous drag or dissipation. As a result, the spreading diameter was smaller when the pore size was smaller for the finer mesh, because the energy was efficiently dissipated. To conclude, the spreading diameter is the largest in the absence of metal meshes, as demonstrated in Fig. 4a. Other than the dissipation of viscous force by the wall, all the initial kinetic energy is smoothly converted to the spreading energy of the liquid film.

Spreading of a drop impacting a mesh with a fiber mat was also studied (not shown); the spreading behavior was only slightly different than that on a mesh without the fiber mat. The slight difference implies that the metal mesh dominates the drop spreading dynamics, thus greatly diminishing the effect of the fiber mat. The spreading radius of a drop on a metal mesh with a fiber mat was slightly smaller than that on a metal mesh only. This smaller spreading radius was caused by the greater viscous drag imposed by the fiber mat. A fiber mat imposes a greater drag force than a solid wall, thus impeding the spreading motion of the liquid. This is demonstrated in Fig. 4c, wherein a smaller spreading diameter is observed than that in Fig. 4a. The maximum spreading diameter was reached at $t = 3$ ms before the edge recedes or recoils with time. However, the spreading liquid travels along the metal fibers while forming lengthy jets around the film periphery. The formation of these lengthy jets is promoted by the liquid pulling. Liquid is easily mobilized along the thin metal fibers via capillary pressure, $\Delta P \sim 2\sigma/R_f$, where R_f is the fiber radius.

Figure 5 compares top views of drops colliding with meshes with fine and medium pores. An air gap of $h_1 = 10$ mm separates the mesh and the solid wall. The air gap was purposely installed in the experiment to simulate the situation described in Fig. 1a, b, wherein drops ejected from a rotating wafer collide with the metal mesh and penetrate them before colliding with the solid wall. The top views show that the drop penetration varies with the pore size of the mesh. In Fig. 5a, the drop passing through the medium-pore-size mesh was found to spread more because of the smaller viscous interference. For the fine mesh with a reduced pore size, the viscous drag is increased because the surface area of the mesh wires in contact with

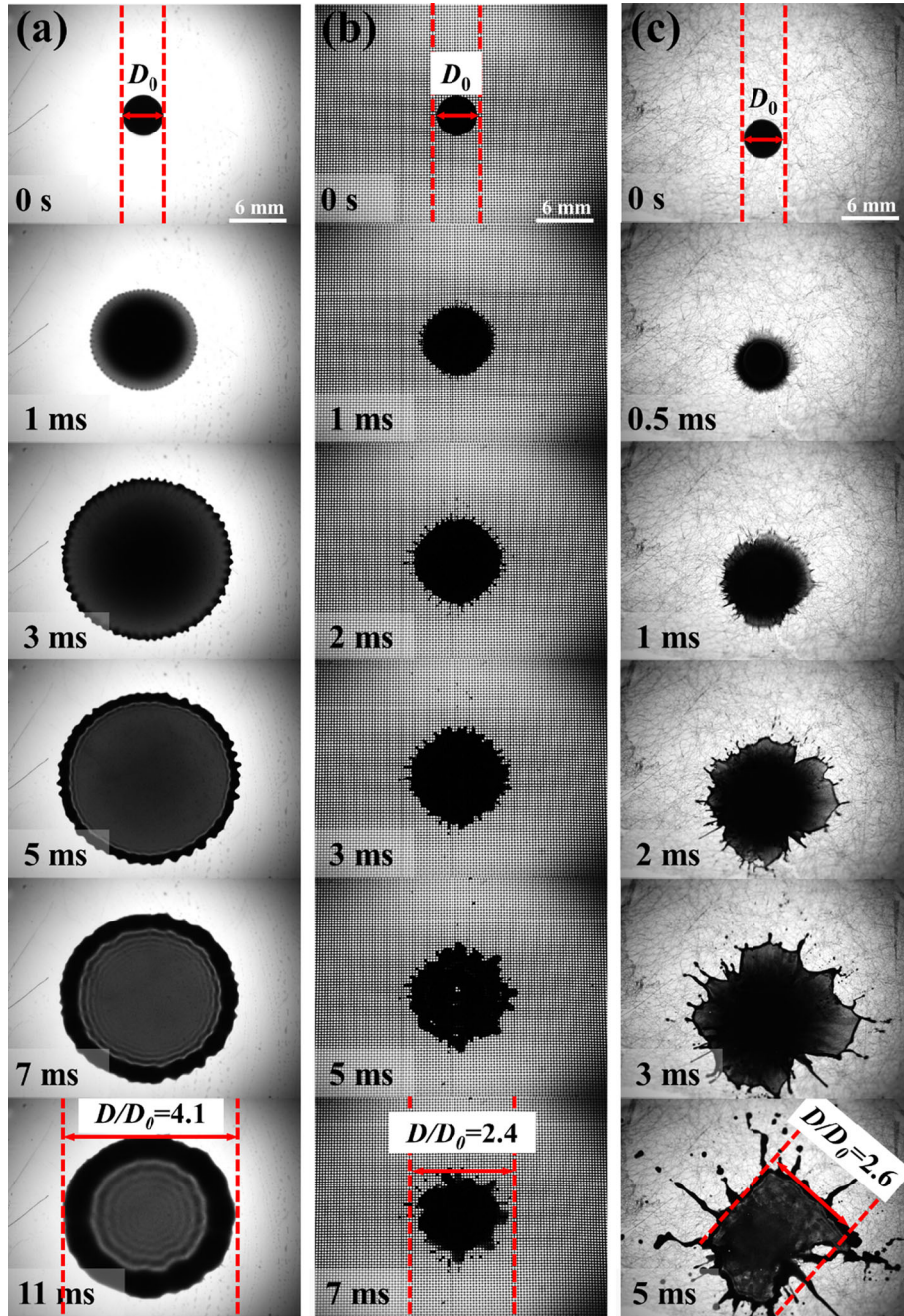


Fig. 4 Single drop impact on **a** a dry wall, **b** fine metal mesh ($\gamma = 1.64$), and **c** metal fiber mat. All impacting conditions were identical for the following three cases: $We = \rho D_0 u_i^2 / \sigma = 553$ and $Re = \rho u_i D_0 / \mu = 12,053$, with $u_i = 3$ m/s, $H_1 = 65$ cm, and $D_0 = 4.5$ mm. No air gap was present between the mesh (mat) and dry wall: $h_1 = 0$ mm

the drop increases. Therefore, after the drop penetrates the mesh, the remaining kinetic energy of the drop is smaller. As a result, the spreading diameter at the solid wall is smaller.

The effect of the fiber mat on drop penetration was also investigated. The fiber mat was installed on metal meshes of different pore sizes and the drop impact behavior was observed (not shown here). Results suggested that the fiber mat had no discernible effect on drop spreading. The liquid breakup through the mesh is essentially dominated by the pore size of the mesh, and the subsequent liquid spreading remains unaffected by the fiber mat. The pore size of the fiber was on the micrometer scale; thus, its presence did not affect the impacting drop because of the dominant millimeter scale of the metal mesh.

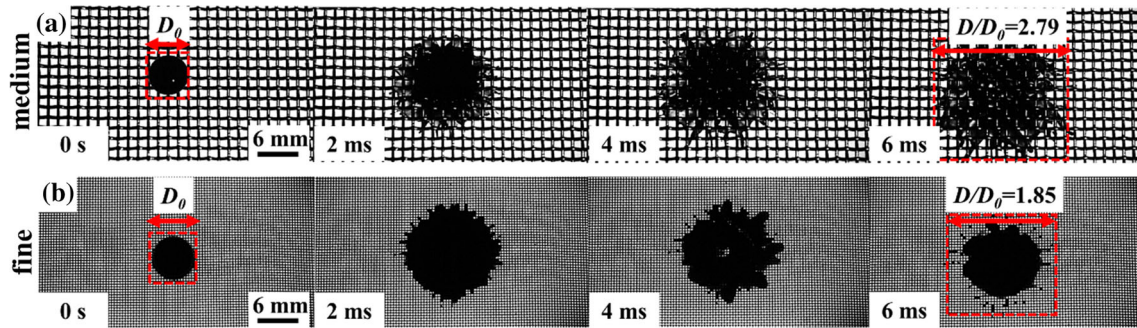


Fig. 5 Time-series snapshots of a single drop colliding with a metal mesh with **a** medium pores ($\gamma = 1.46$) and **b** fine pores ($\gamma = 1.64$). The impacting conditions are $u_i = 3$ m/s, $H_1 = 65$ cm, $D_0 = 4.5$ mm, $We = 553$, and $Re = 12,053$. An air gap of $h_1 = 10$ mm was present between the mesh and solid wall

We introduced a textured metal mesh, as depicted in the inset SEM image in Fig. 1c, to determine the effect of texturing on splashing, which is quantified in Fig. 3 and qualitatively represented in Fig. 2; *no air gap* was present between the mesh (mat) and dry wall. As such, the mesh texturing affects and mitigates the impact of splashing while taking advantage of hydrophilicity of the electroplated mesh. However, when an air gap of $h_1 = 10$ mm was present between the mesh and solid wall, as in Fig. 5, the electroplated mesh exhibited no significant effect on drop penetration and spreading (not shown for brevity). In this *air-gap* scenario represented in Fig. 5, the effect of mesh electroplating is insignificant, unlike the previous case in Figs. 2 and 3, where there was *no air gap* between the mesh and solid wall ($h_1 = 0$ mm). Drop penetration and spreading are essentially governed by the mesh size while the effect of electroplating is obscured and minimized.

Figure 6 compares the effects of the mesh pore size and the use of the fiber mat on drop penetration across the cross section of the mesh. Figure 6a, b shows side views of the drop impact on meshes of medium ($\gamma = 1.46$) and fine ($\gamma = 1.64$) pore sizes, respectively, in conjunction with Fig. 5a, b. Figure 6c also shows side views of the drop impact on a fine mesh covered with a fiber mat. All the meshes were located at $h_1 = 10$ mm from the solid wall; thus, the impacting drop must penetrate the mesh and break up to reach the bottom solid wall.

As shown in the first snapshot in Fig. 5a, the initial drop of $D = 4.5$ mm occupies four cells of the medium-pore-size mesh. At $t = 0.7$ ms in Fig. 6a, the drop is broken into four bulky jets and discharged to reach the bottom. These jets are shaped as continuous columns that do not atomize until they make contact with the wall. After the jet–wall collision, splashed droplets are formed; however, the momentum of these droplets is insufficient to induce rebound to the mesh. The splashed droplets therefore remain within the air gap between the mesh and wall. As mentioned previously, the impacting liquid columns or jets retain sufficient momentum to coalesce and form a liquid film that spreads in the lateral direction, forming a larger spreading diameter, as demonstrated in Fig. 5a. However, when the impacting drop penetrates a fine mesh, ~ 16 columnar jets are formed, which is equal in number to the number of cells occupied by the impacting drop, as shown in the first snapshot in Fig. 5b. These jets are thin enough to undergo the “capillary-driven” Rayleigh–Plateau instability (Rayleigh 1878) and are broken into primary droplets due to necking before droplets reach the bottom solid wall. This jet breakup phenomenon is also referred to as the Rayleigh instability. During the liquid jet breakup, the necking region experiences a high capillary pressure because $\Delta P_{\text{cap}} \sim 2\sigma/R_j$ with decreasing jet radius (R_j). As a result, the volume of the necking region becomes thinner while pushing liquid away from the necking to the bulging region. Thus, the jet eventually breaks up. These atomized droplets are relatively small with insufficient momentum to undergo secondary atomization or breakup. They simply land on the solid wall, form a puddle, and spread, and induces finger formation at the rim or edge of the spreading liquid film. This interfacial phenomenon is known as the “buoyancy-driven” Rayleigh–Taylor instability (Chandrasekhar 1981), which arises when the heavier fluid accelerates toward the lighter fluid or vice versa. However, the film quickly lost momentum and a final spreading diameter of 8.33 cm was recorded, which is about 1.85 times larger than the original drop size of $D_0 = 4.5$ mm. In contrast, the spreading factor of the drop in the case of medium-pore-size mesh was ~ 2.8 ; see Fig. 5a. The larger spreading diameter of the medium-pore-size case indicates the greater momentum remaining after the breakup process while passing through the medium-pore-size metal mesh.

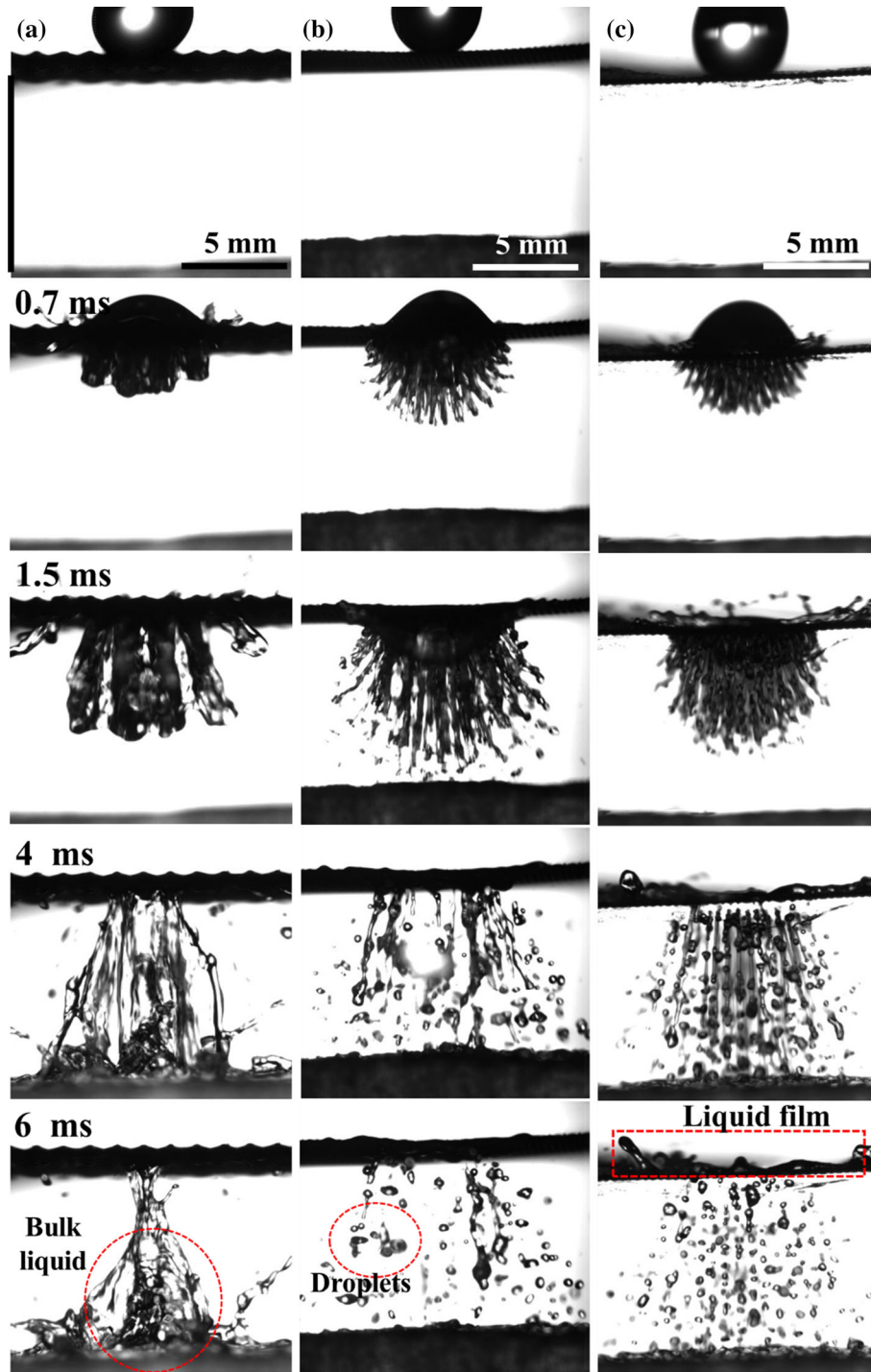


Fig. 6 Time-series snapshots of a single drop ($N = 1$) impacting on a metal mesh with **a** medium ($\gamma = 1.46$) and **b** fine pores ($\gamma = 1.64$); and on **c** a metal mesh with fine pores ($\gamma = 1.64$) covered with a metal fiber mat. The impacting conditions are $u_i = 3$ m/s, $H_1 = 65$ cm, $D_0 = 4.5$ mm, $We = 553$, and $Re = 12,053$. An air gap of $h_1 = 10$ mm was present between the mesh and solid wall

Figure 6c shows the drop impact on a fine mesh covered with a fiber mat. The time-series snapshots are juxtaposed with those from the uncovered fine mesh in Fig. 6b. The final spreading diameters of these two cases are quite similar to that of the top view in Fig. 5b; it seems that the presence of the fiber mat does not affect the overall spreading diameter. However, in the side views shown in Fig. 6b, c, the transient images

differ discernibly. From $t = 0.7$ to 1.5 ms, the jet motion (Fig. 6c) was relatively slow; the presence of the fiber mat impeded the drop penetration. Comparison of the images obtained at $t = 4$ ms indicates that the jets are more uniform when the fiber mat is present. The images at $t = 6$ ms show that the atomized droplets are more uniformly distributed when the fiber mat is present. The presence of the fiber mat moderately affects the drop penetration through the mesh and the breakup of the falling drop. However, it should be reminded that the presence of the fiber mat had no discernible effect on liquid spreading over the substrate. In summary, the drop penetration is moderately affected by the fiber mat presence, but spreading is less likely affected.

Most importantly, a fraction of the falling liquid does not penetrate the mat and remains on top of the mat, as shown in all images in Fig. 6c. The liquid remaining on top rebounds from the mat and produces splashed droplets. These splashed droplets can return to the ejecting wafer location and possibly contaminate the wafer being cleaned. Therefore, the presence of a fiber mat on top of the mesh is undesirable for reducing the amount of splashed droplets at the impact location.

In summary, the pore sizes of the metal wire meshes must be small enough to interfere with the motion of penetrating drops to decrease their kinetic energy and thus minimize the risk of generating splashed droplets. Meanwhile, at the same time, the pore size must be sufficiently large to avoid blockage of the drop by the enhanced surface tension effect owing to the reduced length scale of the interacting structures or geometries.

Figure 7 compares the time-series snapshots of multiple drops ($N = 10$) falling on metal meshes of various pore sizes (coarse, medium, and fine). The falling drop with $D = 4.5$ mm occupies approximately 2, 4, and 16 cells of the coarse, medium, and fine meshes, respectively (Fig. 7a–c).

When the first drop ($N = 1$) impacted the mesh, approximately 2, 4, and 16 jets, respectively, were ejected from the coarse, medium, and fine meshes upon impact (only based on the front views in Fig. 7). Subsequent drops continued to impact the mesh until $N = 10$. The numbers of jets formed do not match the numbers of cells occupied by a single drop; see images for $N \geq 2$ in Fig. 7b, c. The pores of the medium and fine meshes are filled with liquid from the previous drop impact; hence, the drops falling subsequently impact the liquid film formed rather than the dry metal mesh with empty pores. For $N = 10$ in Fig. 7c a single liquid column is formed, indicating that all the pores are filled and connected by liquid. This thin liquid film is formed on the mesh top owing to the enhanced surface tension effect in accordance with the reduced mesh size, and it interferes with the penetration of the following drops. As a result, drop impact on a liquid film promotes splashing significantly, which is undesirable.

However, in case of a mesh with medium pore size, multiple jets still formed below the mesh. The liquid film was no longer prevalent at the mesh top, although some splashed droplets remained. For the largest pore size (coarse mesh; Fig. 7a), the entire volume of the impacting drop penetrated the mesh, and no liquid film formed on top of the mesh, which is the most desirable condition for cleaning a wafer, because it significantly suppresses splashing.

3.2 Horizontal drop impact with air blowing

In another experiment, the wetting percentage of the splashed droplets resulting from multiple-drop impact on the mesh was quantified. Multiple drops were released from a rotating wafer, as shown in Fig. 1b. When the wafer rotation speed was 300 rpm, the speed of the ejecting drops at the edge of the rotating wafer was estimated to be $u_i = 2.5$ m/s, based on the images acquired from the high-speed video.

Water-sensitive papers were located at $3 \leq d_2 \leq 13$ cm from the impacting location. Air was blown in a vertical direction (from top to bottom) to sweep away or intercept splashed droplets traveling horizontally. The blown air was provided by a supersonic nozzle at pressures of 1–5 bar; greater pressure corresponds to greater blowing speed according to the isentropic 1D flow theory (Shapiro 1953). At higher blowing speeds, the air sweeps away the splashed droplets more efficiently. However, an excessive blowing speed can cause secondary atomization or breakup of the splashed droplets (Lefebvre 1988). This secondary breakup can produce more droplets and increase the risk of contamination. Figure 8a compares the amount of splashed droplets qualitatively. For the scenario *without* air blowing, a greater number of splashed droplets travelled back to the wafer. *With* air blowing, the splashed droplets were efficiently swept away, and fewer splashed droplets travelled back to the wafer. Figure 8b quantitatively compares the amount of splashed droplets as a function of blowing pressure or air speed. It appears that blowing air at a pressure of 3 bar is optimal for suppressing splashing.

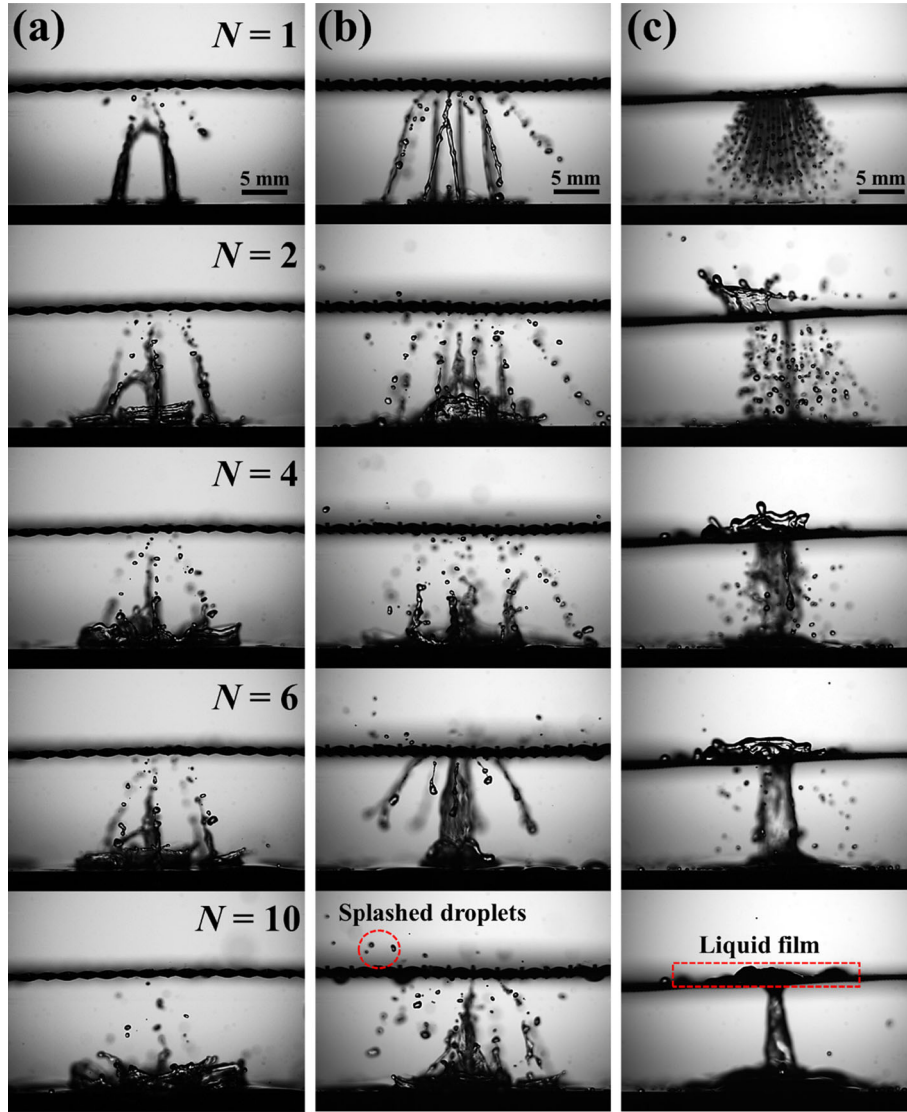


Fig. 7 Time-series snapshots of multiple drops ($N = 10$) impacting a metal mesh with **a** coarse ($\gamma = 1.29$), **b** medium ($\gamma = 1.46$), and **c** fine ($\gamma = 1.64$) pores. The Reynolds and Weber numbers are $We = 553$ and $Re = 12,053$. An air gap of $h_1 = 10$ mm was present between the mesh and solid wall

These trends are correlated by the quadratic functions below for w/o nozzle, 1 bar, 3 bar, and 5 bar, respectively, in conjunction with Fig. 8b

$$W_1 = 0.14d_2^2 - 6.52d_2 + 63.59 \quad (4)$$

$$W_2 = 0.31d_2^2 - 7.59d_2 + 47.39 \quad (5)$$

$$W_3 = 0.15d_2^2 - 4.1d_2 + 29.29 \quad (6)$$

$$W_4 = 0.14d_2^2 - 4.1d_2 + 29.29 \quad (7)$$

Figure 8c compares the effect of the number of mesh layers on splashing. Meshes with medium pores were used and the air was blown at a pressure of 3 bar. The solid wall was located 2 cm away from the single mesh. For the double-mesh case, an additional mesh was inserted midway between the first mesh and solid wall. The differences are quantitatively compared in Fig. 8d. The most effective suppression of splashing was observed with the double mesh. Drops penetrated the first mesh and then experienced additional reduction in speed as they penetrated the second mesh. Thus, the kinetic energy of the impacting

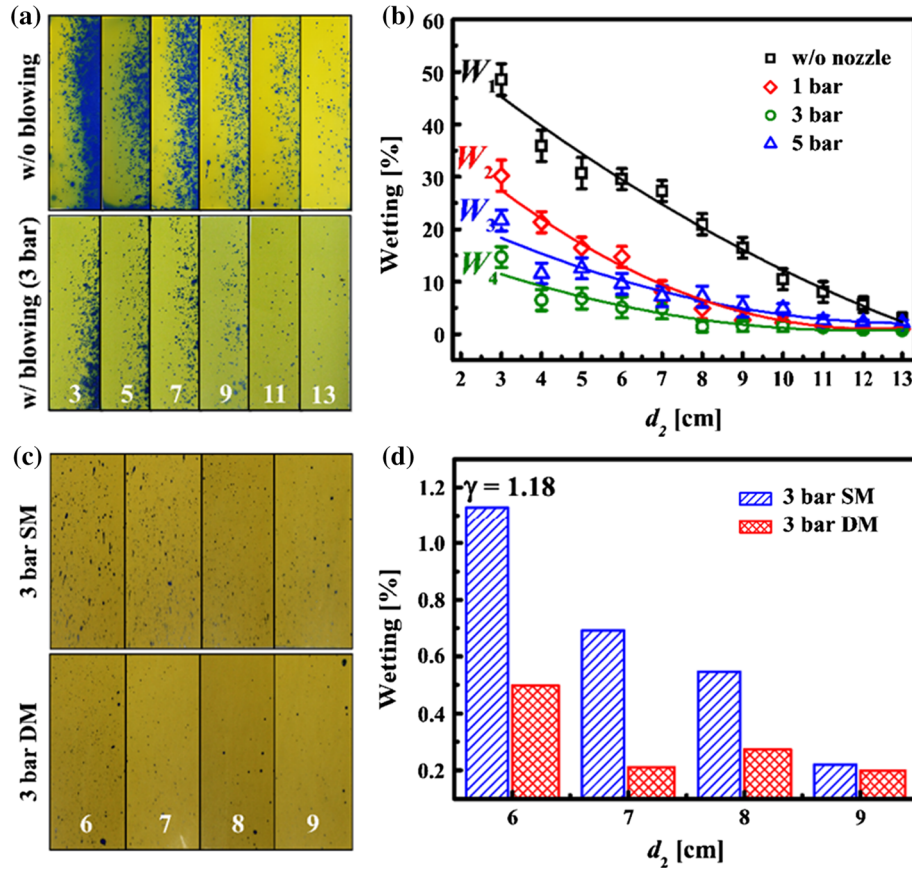


Fig. 8 **a** Water-sensitive papers placed at various locations with respect to the impacting location ($3 \leq d_2 \leq 13$ cm) *without* (top) and *with* (bottom) air blowing. No metal mesh was used. **b** Wetting percentages for various blowing conditions derived from **a**. **c** Water-sensitive papers placed at various distances ($6 \leq d_2 \leq 9$ cm) with respect to the impacting location with air-blowing (3 bar); a single or double metal mesh was used ($\gamma = 1.18$). **d** Wetting percentages derived from **c**. The wafer rotating speed is 300 rpm, yielding $u_i = 2.5$ m/s

liquid was greatly reduced by the time it reached the solid wall. As the bouncing splashed droplets would have insufficient momentum to travel back to the rotating wafer, the wafer contamination would be greatly reduced.

Figure 9 compares the wetting percentages of the splashed droplets *without* a mesh, *with* a mesh, *with* a mesh/mat, and *with* mesh/blowing at 3 bar at an increased rotating speed of 500 rpm and the drop impact speed of $u_i = 4.1$ m/s, estimated from the high-speed video images. These trends are correlated by the quadratic functions below for w/o mesh, mesh, mesh/mat, and mesh/3 bar, respectively, in conjunction with Fig. 9b

$$W_1 = -0.31d_2^2 + 2.68d_2 + 50.49 \quad (8)$$

$$W_2 = 0.46d_2^2 - 9.7d_2 + 58.68 \quad (9)$$

$$W_3 = 0.24d_2^2 - 5.22d_2 + 31.69 \quad (10)$$

$$W_4 = 0.41d_2^2 - 9.71d_2 + 66.43 \quad (11)$$

The greatest wetting percentage was achieved when no mesh was used and the smallest wetting was observed when a mesh was used along with air blowing at a pressure of 3 bar. We have previously demonstrated that splashing is promoted when a fiber mat is installed on the mesh top, which is not desirable. The reduced mesh size increased the surface tension force ($\Delta P \sim 2\sigma/R_{\text{mesh}}$), which in turn held the liquid along the wires of the mesh and fiber mat. Drops adhere and tangle on the mesh and fiber mat, exhibiting the surface tension effect. This excessively saturated pool caused the formation of a liquid pool on the mesh or/and mat, which is demonstrated in Figs. 9c and 10; also see MOVIE S1.

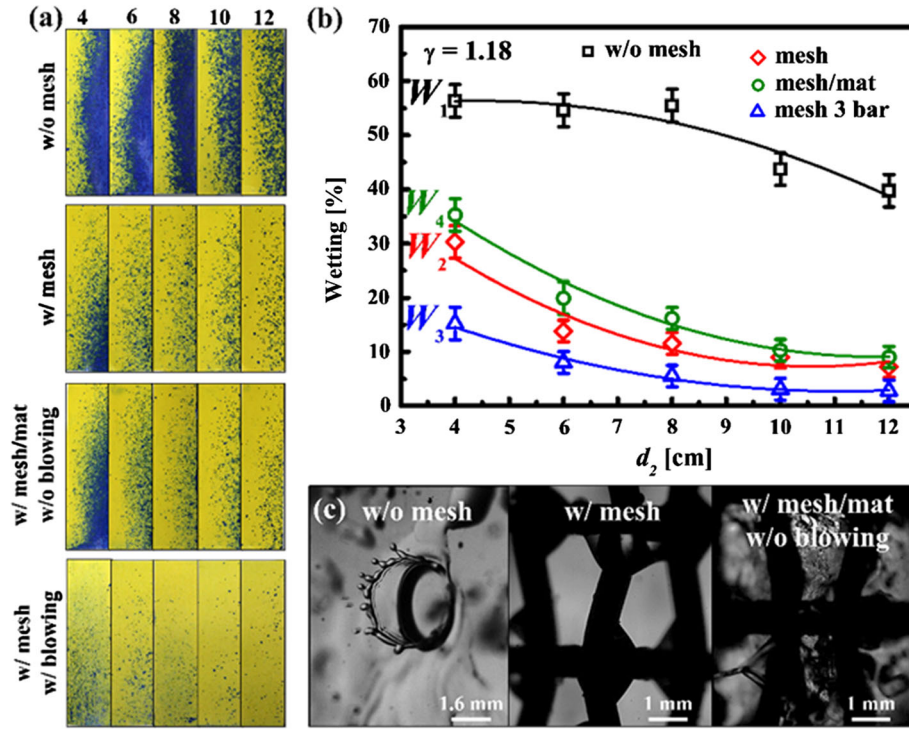


Fig. 9 **a** Water-sensitive papers placed at various locations from the impacting location ($4 \leq d_2 \leq 12$ cm) *without* a mesh, *with* a mesh, *with* a mesh/mat, and *with* mesh/blowing. A mesh with *medium* pore size was used. **b** Wetting percentages corresponding to **a**. **c** Snapshots corresponding to **a** and **b**. The wafer rotation speed was 500 rpm, yielding $u_t = 4.1$ m/s. The geometric ratio of the medium mesh is $\gamma = 1.18$

Figure 10 shows the impact phenomena on various impact surfaces. In Fig. 10a, on the vertically oriented solid wall, thin liquid films are attached to the wall, onto which drops collide and splash. These liquid films or puddles stick to the wall because of surface tension and do not drip vertically. A drop size of $D = 0.47$ mm collides with the wet wall, inducing a typical milk-crown splashing that generates multiple splashed droplets at the rim. These splashed droplets travel back to the rotating wafer horizontally, thus increasing the wafer contamination.

In Fig. 10b, drops collide with the mesh. Simultaneously, some smaller drops immediately pass through the mesh pores. Upon impact, some splashed droplets retain their momentum and pass through the mesh in the horizontal direction. However, some droplets bounce back in the upstream direction. Meanwhile, some splashed droplets adhere to the mesh wire surface under liquid surface tension. The accumulated liquid at the wires dangles until its weight overcomes the surface tension; see the snapshots for $t \geq 2$ ms in Fig. 10b. At this point, the dangling liquid finally drips and clears the pores. Simultaneously, some pores remain completely filled with liquid, in which case the incoming drops land on the liquid pool, which induces splashing. The formation of liquid pools across the pores increases with decreasing pore size (for finer pores), because the surface tension effect is stronger for materials with reduced characteristic length scales; see MOVIE S1.

We have previously demonstrated in Fig. 9b that the fiber mat does not help in reducing splashing. This is because the pores in the fiber mat were of micrometer scale, which dramatically increased the surface tension effect. In Fig. 10c, the formation of the liquid film across the fiber mat is clear. In Fig. 6c, we showed that the impacting drop did not penetrate the fiber mat completely, leaving some liquid that formed a liquid film on the top of the fiber mat. Subsequent drops therefore impacted the liquid film, rather than impacting the dry mesh that would have allowed smooth filtration of the incoming drops. Because of this enhanced surface tension force with a finer mesh or/and a fiber mat, splashing is promoted, which is undesirable for wafer cleaning.

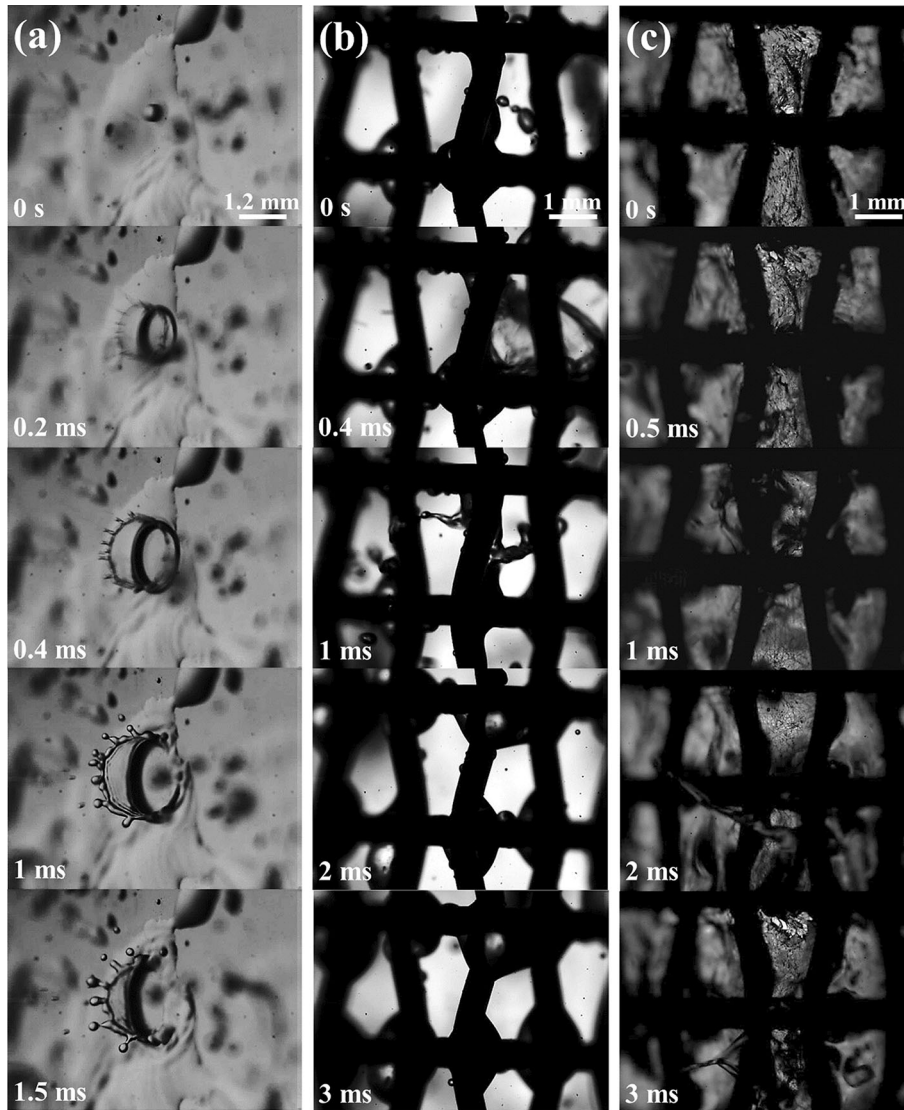


Fig. 10 Time-series snapshots of impacting drops on a **a** solid wall, **b** metal mesh, and **c** mesh covered with a fiber mat. The impacting drops were ejected from a rotating wafer (500 rpm) that yields an impact speed of $u_i = 4.1$ m/s. The geometric ratio of the medium mesh is $\gamma = 1.18$

3.3 Effect of mesh wire size and layer number

Figure 11 compares the effect of the geometric ratio γ and the number of mesh layers (single, double, triple, and quadruple or $N_m = 1, 2, 3,$ and 4) on the wetting percentage. Meshes with pore sizes D_p of 0.97, 1.72, 1.09, and 0.22 mm and wire diameters D_w of 0.18, 0.5, 0.5, and 0.14 mm yield the corresponding geometric ratios $\gamma = 1.18, 1.29, 1.46,$ and $1.64,$ respectively. As shown in Fig. 11a, b, at 300 rpm, a smaller γ produces a lower wetting percentage, which is desirable. These trends are correlated by the quadratic functions below for $\gamma = 1.64, 1.46, 1.29,$ and $1.18,$ respectively, in conjunction with Fig. 11b

$$W_1 = 0.11d_2^2 - 6.06d_2 + 59.76 \quad (12)$$

$$W_2 = 0.25d_2^2 - 7.64d_2 + 59.35 \quad (13)$$

$$W_3 = 0.08d_2^2 - 1.82d_2 + 11.62 \quad (14)$$

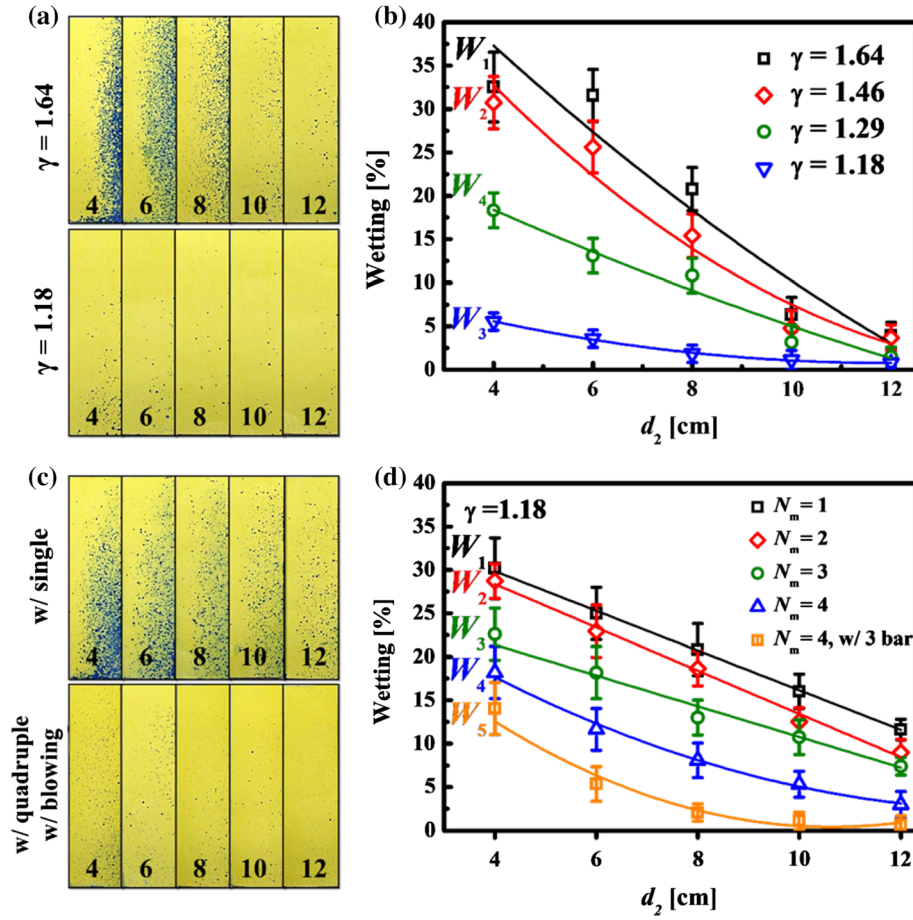


Fig. 11 a, b Water-sensitive papers and wetting percentages at various locations ranging $4 \leq d_2 \leq 12$ cm for various mesh sizes ($\gamma = 1.64, 1.46, 1.29$, and 1.18). Note that the rotation speed was 300 rpm and a single mesh was employed for all cases. c, d Water-sensitive papers and wetting percentages at various locations ranging $4 \leq d_2 \leq 12$ cm for various numbers of meshes; $N_m = 1, 2, 3, 4$, and 4 w/ with air-blowing. Note that the rotation speed was 500 rpm

$$W_4 = 0.05d_2^2 - 2.89d_2 + 29.21 \quad (15)$$

It is noteworthy that the wetting percentages for $\gamma = 1.18$ and 1.46 are drastically different, although the pore sizes are approximately the same ($D_p = 0.97$ and 1.09). The smaller wire size of the $\gamma = 1.18$ case leads to a smaller contact area between the impacting drops and wire, thereby minimizing splashing.

Figure 11c, d compares the effect of the number of mesh layers on the extent of wetting with the disk rotating speed of 500 rpm. A mesh with greater number of layers yielded lesser splashing, which is desirable. This suggests that multiple layers behind the first mesh layer slow the impacting drops much more significantly with increased drag. Thus, increasing the drag by employing increased number of wires is favorable. However, increasing the drag by increasing the wire size (D_w) would only induce an unfavorable effect because it increases γ . Figure 11c qualitatively elucidates the benefit of employing multiple meshes along with supersonic blowing. The effect of blowing on reducing the wetting for a wide d_2 range, $4 \leq d_2 \leq 12$ cm, is evident. These trends are correlated by the quadratic functions below for or $N_m = 1, 2, 3, 4$, and 4 w/3 bar, respectively, in conjunction with Fig. 11d

$$W_1 = 2.28d_2 + 38.98 \quad (16)$$

$$W_2 = -2.49d_2 + 38.31 \quad (17)$$

$$W_3 = -1.76d_2 + 28.44 \quad (18)$$

$$W_4 = 0.14d_2^2 - 4.11d_2 + 31.83 \quad (19)$$

$$W_5 = 0.27d_2^2 - 5.87d_2 + 31.63 \quad (20)$$

In summary, reducing the wire size and/or increasing the pore size is favorable to minimize splashing, because the corresponding mesh geometry minimizes the impacting area for the incoming drops. However, increasing the number of wires behind the first impacting mesh is also favorable in reducing splashing because multiple wires slow the impacting drops through increased drag.

4 Conclusion

Collision of drops ejected from a rotating wafer on a dry wall or metal meshes of various pore sizes with and without metal fiber mats was studied. These obstacles (metal meshes) were introduced deliberately to intercept the drop before it collides the solid wall. They interfered with the drop motion and slowed the drop speed before impact, thereby minimizing the splashing of drops to produce droplets. For the vertical impact scenarios ($h_1 = 0$ mm), the wetting percentage was less than 1% even when the impact height was the highest ($H_1 = 65$ cm) using the double electroplated meshes ($\gamma = 1.46$). Essentially all splashing was suppressed. For $h_1 = 10$ mm, the drop penetration phenomena were influenced by γ . However, γ had an insignificant effect on subsequent drop spreading. For the horizontal impact scenarios (300 rpm), the wetting percentage decreased from $W = 49\%$ to 14% at $d_2 = 3$ cm by simple supersonic blowing (3 bar) without using a mesh. When a mesh of $\gamma = 1.18$ was used, the wetting percentage decreased less than 1%. For a higher impact speed of 500 rpm, the wetting percentage decreased from 56% (no mesh) to 15% when a mesh ($\gamma = 1.18$) and air blowing at 3 bar were applied.

A mesh with a finer pore size prevented drops from completely penetrating, because the greater drag imposed on the penetrating drop caused some liquid mass to remain on top of the mesh or/and fiber mat. Thus, incoming drops landed on a liquid pool formed on the mesh/mat top, which enhanced splashing. The splashed droplets traveled back toward the wafer and thus increased the risk of re-contamination. We also found that a smaller $\gamma = 1.18$ value yielded a lesser wetting percentage. This implies that a smaller wire thickness or/and larger pore size is favorable for reducing splashed droplets. However, a mesh with an excessively large pore size would allow drops to simply pass through the pores and the drops would not be slowed. That is, the blocking role of the mesh would be eliminated. Therefore, the pore size should be sufficiently small to hinder the motion of the incoming drops but at the same time be large enough to permit smooth filtration of the drops, which would minimize the formation of a liquid film and subsequent splashing.

Acknowledgements This research was supported by the Technology Development Program to Solve Climate Changes of the National Research Foundation (NRF) funded by the Ministry of Science, ICT and Future Planning (NRF-2016M1A2A2936760), NRF-2017R1A2B4005639, and NRF-2013R1A5A1073861. This research is also funded by King Saud University, Riyadh, Saudi Arabia, Researchers Supporting Project (RSP-2019/30).

References

- An S, Lee C, Liou M, Jo HS, Park J-J, Yarin AL et al (2014) Supersonically blown ultrathin thorny devil nanofibers for efficient air cooling. *ACS Appl Mater Interfaces* 6(16):13657–13666
- An S, Jo HS, Kim DY, Lee HJ, Ju BK, Al-Deyab SS et al (2016) Self-junctioned copper nanofiber transparent flexible conducting film via electrospinning and electroplating. *Adv Mater* 28(33):7149–7154
- Boscariol C, Chandra S, Sarker D, Crua C, Marengo M (2018) Drop impact onto attached metallic meshes: liquid penetration and spreading. *Exp Fluids* 59(12):189
- Chandrasekhar S (1981) *Hydrodynamic and hydromagnetic stability*. Dover Publications, Mineola
- Drazin PG, Reid WH (2004) *Hydrodynamic stability*. Cambridge University Press, Cambridge
- Hattori T, Osaka T, Okamoto A, Saga K, Kuniyasu H (1998) Contamination removal by single-wafer spin cleaning with repetitive use of ozonized water and dilute HF. *J Electrochem Soc* 145(9):3278–3284
- Kern W (1990) The evolution of silicon wafer cleaning technology. *J Electrochem Soc* 137(6):1887–1892
- Kim M-w, Yoon H, Ohm TY, Jo HS, An S, Choi SK et al (2017) Nanotextured cupric oxide nanofibers coated with atomic layer deposited ZnO-TiO₂ as highly efficient photocathodes. *Appl Catal B Environ* 201:479–485
- Kim T-G, Lee J-G, Park C-W, Jo H-S, Kim M-W, van Hest MF et al (2018) Effect of supersonic spraying impact velocity on opto-electric properties of transparent conducting flexible films consisting of silver nanowire, ITO, and polyimide multilayers. *J Alloys Compd* 739:653–659

- Lee JG, Kim D-Y, Lee J-H, Kim M-w, An S, Jo HS et al (2016) Scalable binder-free supersonic cold spraying of nanotextured cupric oxide (CuO) films as efficient photocathodes. *ACS Appl Mater Interfaces* 8(24):15406–15414
- Lee JG, Kim DY, Lee JH, Sinha-Ray S, Yarin AL, Swihart MT et al (2017) Production of flexible transparent conducting films of self-fused nanowires via one-step supersonic spraying. *Adv Funct Mater* 27(1):1602548
- Lefebvre A (1988) *Atomization and sprays*. Begell House, Danbury
- Lembach AN, Tan H-B, Roisman IV, Gambaryan-Roisman T, Zhang Y, Tropea C et al (2010) Drop impact, spreading, splashing, and penetration into electrospun nanofiber mats. *Langmuir* 26(12):9516–9523
- Rayleigh L (1878) On the instability of jets. *Proc Lond Math Soc* s1-10(1):4–13
- Ruzyllo J, Hattori T (2014) Preface to the focus issue on semiconductor surface cleaning and conditioning. *ECS J Solid State Sci Technol* 3(1):Y1
- Ruzyllo J, Hattori T, Novak RE, Mertens P, Besson P (2007) Evolution of silicon cleaning technology over the last twenty years. *ECS Trans* 11(2):3–7
- Ryoo K (2005a) Characteristics of electrolyzed anode water as a display cleaning medium. *Met Mater Int* 11(4):295–299
- Ryoo K (2005b) Metal oxide particle removal using electrolyzed anode water. *J Electrochem Soc* 152(11):G885–G888
- Ryu S, Sen P, Nam Y, Lee C (2017) Water penetration through a superhydrophobic mesh during a drop impact. *Phys Rev Lett* 118(1):014501
- Sahu RP, Sinha-Ray S, Yarin A, Pourdeyhimi B (2012) Drop impacts on electrospun nanofiber membranes. *Soft Matter* 8(14):3957–3970
- Sahu R, Sinha-Ray S, Yarin A, Pourdeyhimi B (2013) Blowing drops off a filament. *Soft Matter* 9(26):6053–6071
- Sahu R, Sett S, Yarin A, Pourdeyhimi B (2015) Impact of aqueous suspension drops onto non-wettable porous membranes: hydrodynamic focusing and penetration of nanoparticles. *Colloids Surf A Physicochem Eng Asp* 467:31–45
- Sato N, Yamazaki O, Shimogaki Y (2012) Impacts of chemical supply flow on particle removability in wet clean bath. *J Electrochem Soc* 159(4):H367–H372
- Shapiro AH (1953) *The dynamics and thermodynamics of compressible fluid flow*, vol 1. Ronald Press, New York
- Xu J, Xie J, He X, Cheng Y, Liu Q (2017) Water drop impacts on a single-layer of mesh screen membrane: effect of water hammer pressure and advancing contact angles. *Exp Therm Fluid Sci* 82:83–93
- Yoon H, Kim M-w, Kim H, Kim D-Y, An S, Lee J-G et al (2016) Efficient heat removal via thorny devil nanofiber, silver nanowire, and graphene nanotextured surfaces. *Int J Heat Mass Transf* 101:198–204
- Zhang G, Quetzeri-Santiago MA, Stone CA, Botto L, Castrejón-Pita JR (2018) Droplet impact dynamics on textiles. *Soft Matter* 14(40):8182–8190